Available online at www.sciencedirect.com
SCIENCE DIRECT®
International Journal of Solids and Structures 42 (2005) 159–185
INTERNATIONAL JOURNAL OF SOLIDS and STRUCTURES
www.elsevier.com/locate/ijsolstr

A new variable-order singular boundary element for calculating stress intensity factors in three-dimensional elasticity problems

W. Zhou [a], K.M. Lim [b,*], K.H. Lee [b], A.A.O. Tay [b]

[a] *R&D, Micron Semiconductor Asia Pvt. Ltd., 990 Bendemeer Road, Singapore 339942*
[b] *Mechanical Engineering Department, National University of Singapore, 9 Engineering Drive 1, Singapore 117576*

Received 9 December 2003; received in revised form 22 July 2004
Available online 15 September 2004

Abstract

A new three-dimensional variable-order singular boundary element has been constructed for stress analysis of three-dimensional interface cracks and internal material junctions. The singular fields in the vicinity of crack front or junction have been accurately represented by the singular elements by taking account the variable order of singularities and the angular profiles of field variables. Both the singular stress fields and displacement fields are independently formulated by the element's shape functions. Different kinds of displacement formulations are investigated. The formulation combining singular and linear terms is found to be the most accurate one. The mixed-mode stress intensity factors are treated as nodal unknowns. The variation of stress intensity factors along the line of singularity can be obtained directly from the final system of equations and thus no post processing, such as three-dimensional J-integral or domain integral, is necessary. Numerical examples involving stress singularity, such as penny-shaped cracks in homogeneous and dissimilar material interface, plates with through-thickness cracks, and a dissimilar inclusion, are investigated. The analysis results are in good agreement with those reported in the literature.

Keywords: 3D singular elements; Boundary element method; Stress intensity factors; Stress singularity

* Corresponding author. Tel.: +65 6874 8860; fax: +65 6779 1459.
E-mail address: limkm@nus.edu.sg (K.M. Lim).

0020-7683/$ - see front matter © 2004 Elsevier Ltd. All rights reserved.
doi:10.1016/j.ijsolstr.2004.07.017

1. Introduction

Stress singularity problems often occur in structures where the geometry undergoes sharp changes. Typical examples include cracks and dissimilar material corners. In each of these cases, the singular stress fields are generally three-dimensional in character. The fracture parameter, such as the stress intensity coefficient, is a function of the position on the line of singularity and not a single constant as in the case of two-dimensional singularity problems. This line of singularity is a locus of singularity points which may be a crack front or an interior edge of a dissimilar material corner.

Three-dimensional stress problems due to singularities have not been investigated as extensively as their two-dimensional counterparts. This is possibly due to the complexity in the formulation of the problems, the requirement of large computer resources for numerical calculations, and the lack of efficient methods to provide accurate results. Among the methods used for studying three-dimensional stress singularity problems and calculating fracture parameters, the finite element method (FEM) together with domain integrals is commonly used to extract the results for the energy release rate. Excellent review papers on this subject have been written by Moran and Shih (1987a,b). This method was employed by Li et al. (1985), and further improved by Shih and Asaro (1988) using interaction energy integrals to extract mixed mode stress intensity factors for planar crack problems. Nakamura and Parks (1988, 1989) have used the same approach to analyze a thin elastic plate with a through-thickness crack for symmetrical and anti-symmetrical modes. Kwon and Sun (2000) investigated a similar thin elastic cracked-plate and indicated the relationship between 3D stress intensity factors at the midplane and 2D plane stress results. Gosz et al. (1998) also used the same method to calculate complex stress intensity factors for curved three-dimensional interface cracks. All these analyses used an extremely fine finite element mesh in the vicinity of the crack front to determine the displacement and stress fields. Post-processing techniques which usually involve the evaluation of some energy integrals, such as the J-integral (Moran and Shih, 1987a), are then used to extract point-wise fracture parameters along the crack front. Sub-modeling techniques are often used to achieve the fine mesh in the vicinity of the crack front and this requires a very high computational cost. Also, this method is only applicable to crack problems and it cannot be used for more general stress singularity problems such as corners of bimaterial inclusions or multi-material junctions.

Special crack-tip elements have been developed for the FEM to replace conventional elements for evaluating the singular stress state in the vicinity of the crack front. Quarter-point elements that are easily implemented by shifting the mid-side nodes are proposed to include the square-root displacement field at the crack front (Henshell and Shaw, 1975; Barsoum, 1976). Tracey and Cook (1977) created a triangular element incorporating the correct order of singularity originating at one node of the element. Lim and Kim (1994) proposed a variable-order singular finite element to simulate the variable orders of singularity by adjusting the location of the mid-side nodes. Their formulation is applied to cracks terminating at bimaterial interfaces. Pageau and Biggers (1997) employed enriched finite elements to analyze the singular stress fields for three-dimensional crack problems. However, a high computational cost is still incurred due to the complexities in three-dimensional stress problems.

In recent years, the boundary element method (BEM) provides an attractive alternative to the FEM in the analysis of crack problems. The advantages of BEM over FEM are particularly important for three-dimensional singularity problems. The dimension of the problem is reduced by one since only variables on the boundary, instead of the interior, are used in the formulation. The solution for the boundary variables is normally sufficient for most problems since the peak stresses usually occur on the boundary. The BEM also provides a direct evaluation of the stresses on the boundary, while the FEM needs extrapolation of the results from interior Gauss points. For the BEM, the displacements and tractions are considered as the primary variables and they may use different shape functions. Both these quantities are thus evaluated directly in the BEM, in contrast with the displacement-based FEM where the stresses are derived from the displacements at a later stage. The BEM has been regarded as more capable of solving crack problems

(Cruse and Vanburen, 1971; Aliabadi, 1997). However, in the conventional BEM, a fine mesh is still needed in the vicinity of the crack front for analysis if normal quadratic boundary elements are used. Furthermore, these elements cannot deal with unbounded discontinuous tractions occurring at a corner due to the abrupt change of the normal to the boundary (Walker and Fenner, 1989). Special treatments have been proposed, for example, by using a small curved boundary to replace the corner or using a discontinuous boundary element (Mustoe, 1980; Aliabadi, 1997). Quarter-point singular boundary elements (Tan and Gao, 1990; Gray et al., 2003) were also developed to accurately model the near crack tip displacement and traction fields. However, these elements are generally designed for the square-root singularity fields near the crack tip and may not handle general singularity orders other than half.

In this paper, a new variable-order singular boundary element is formulated to resolve the above-mentioned difficulties for three-dimensional stress problems. This is an extension of the formulation for two-dimensional stress singularity problems presented by Lim et al. (2002). The singular field in the vicinity of the line of singularity is assumed to be dominated by a combination of two in-plane and one out-of-plane singular modes, with the stress intensity coefficients varying along the line of singularity. The variable orders and angular field profiles are obtained separately from asymptotic singularity analysis. These asymptotic solutions form the basis of the shape functions in the new singular elements. Both asymptotic stress and displacement fields are represented simultaneously for a better accuracy even in a very coarse mesh. The new singular surface elements replace the conventional elements adjacent to the line of singularity. Transition elements are not required because the singular elements are made naturally compatible with adjacent normal quadratic boundary elements. This formulation also resolves the difficulties encountered at a corner or edge where the traction field is discontinuous since the stress intensity factors and asymptotic fields rather than the tractions are explicitly represented at the corner. The stress intensity factors are formulated as nodal unknowns along the line of singularity and they can be directly obtained from the solution process. The post-processing step commonly used in the literature, is not necessary in this case.

2. Near-tip asymptotic singularity analysis

This section describes the method to obtain the singularity fields along the line of singularities. Fig. 1 shows a curvilinear crack front with the crack face on the inside region and the bonded face on the outside region. A local orthogonal coordinate system is set up at point O along the crack front such that the y'-axis is perpendicular to the plane of the crack, and the x'- and z'-axes, lying in the plane of the crack, are normal and tangential to the crack front, respectively. Hartranft and Sih (1969) employed the asymptotic series expansion in three-dimensions and showed that the near-tip behavior of the three-dimensional field in the plane normal to crack front is identical to the two-dimensional plane strain field. However, the magnitudes of the singularities, that is, the stress intensity factors, vary with the position O on the crack front.

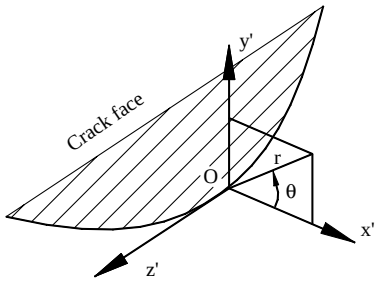

Fig. 1. Local coordinate system along curved crack front.

This conclusion was used by many researchers to perform the analysis of three-dimensional crack problems (Pageau and Biggers, 1997; Gosz et al., 1998; Cisilino and Aliabadi, 1999). Nakamura and Parks (1988) and Kwon and Sun (2000) calculated an index of plane strain in the vicinity of the crack front numerically and found that the index near the crack front is almost equal to unity, verifying the plane strain assumption. In the current work, the near-tip singular field is assumed to be dominated by three singular modes: two in-plane modes with the plane strain assumption, commonly known as mode I (opening) and mode II (shearing), and one out-of-plane mode, commonly known as mode III (shearing). It should be noted that, even with the provision of a variation in the stress intensity factors along the crack front, the current formulation is not applicable to the corner where the crack front intersects with the free surface. This is due to the presence of a corner singularity which has a different order (Benthem, 1977). The treatment of this corner singularity is beyond the scope of this paper, and it will be examined in detail in the future work. For the analysis in this paper, the effect of the corner singularity is neglected since it is only restricted to a small region around the corner.

In the vicinity of a point on the line of singularity for a three-dimensional stress singularity problem, the stress fields and displacement fields can be written in terms of asymptotic solutions as

$$u = \sum_{h=1}^{s} C_h r^{\lambda_h} f_h(\theta) \tag{1}$$

$$\sigma = \sum_{h=1}^{s} C_h r^{\lambda_h - 1} g_h(\theta) \tag{2}$$

where u and σ are the displacement vector and stress tensor, respectively, r is the distance between singularity tip O and the point of interest in the normal plane $Ox'y'$, λ_h is the hth order of singularity, h represents the order of the mode (I, II or III), θ is the angle between x-axis and the radial line to the point of interest in the normal plane Oxy, $f_h(\theta)$ and $g_h(\theta)$ are the tensors giving the angular profiles of the displacements and stresses, respectively, and C_h are the stress intensity coefficients. Analyses show that the order for mode III is generally a real number which suggests that the corresponding stress intensity coefficient C_{III} is also real. However, for the two in-plane modes (I and II), the orders of singularities may be real numbers or complex numbers, depending on actual geometry and material configurations. If the orders of modes I and II are two real numbers, the two corresponding stress intensity coefficients C_{I} and C_{II} are also real. If modes I and II are governed by a pair of complex orders, their corresponding stress intensity coefficients are conjugate to each other (Lim et al., 2002). Hence, in the case where C_{I} and C_{II} are a pair of conjugate complex stress intensity coefficients, their real and imaginary parts are used as two independent real unknowns instead. Thus, there are always only three independent real components of stress intensity coefficients associated with any singular point along the line of singularities. These three real components are represented by K_h ($h = \mathrm{I}, \mathrm{II}, \mathrm{III}$), to differentiate from the possible complex coefficients C_h. In the following sections, the formulations are written based on the real variable-orders for a clearer illustration. The formulation corresponding to complex orders of singularities follows a similar fashion except for slight variations in handling real and imaginary components of the field variables.

The general asymptotic displacement and stress fields near tip O along the line of singularity for the three-dimensional stress singularity problem are given in Eqs. (1) and (2), respectively. Considering the superposition of the three modes (I, II and III), Eqs. (1) and (2) can be written explicitly as

$$\begin{pmatrix} u_x \\ u_y \\ u_z \end{pmatrix} = K_{\mathrm{I}} r^{\lambda_{\mathrm{I}}} \begin{pmatrix} f_{\mathrm{I}x}(\theta) \\ f_{\mathrm{I}y}(\theta) \\ 0 \end{pmatrix} + K_{\mathrm{II}} r^{\lambda_{\mathrm{II}}} \begin{pmatrix} f_{\mathrm{II}x}(\theta) \\ f_{\mathrm{II}y}(\theta) \\ 0 \end{pmatrix} + K_{\mathrm{III}} r^{\lambda_{\mathrm{III}}} \begin{pmatrix} 0 \\ 0 \\ f_{\mathrm{III}z}(\theta) \end{pmatrix} \tag{3}$$

$$\begin{bmatrix} \sigma_{xx} & \sigma_{xy} & \sigma_{xz} \\ \sigma_{xy} & \sigma_{yy} & \sigma_{yz} \\ \sigma_{xz} & \sigma_{yz} & \sigma_{zz} \end{bmatrix} = K_{\mathrm{I}} r^{\lambda_{\mathrm{I}}-1} \begin{bmatrix} g_{\mathrm{I}xx}(\theta) & g_{\mathrm{I}xy}(\theta) & 0 \\ g_{\mathrm{I}xy}(\theta) & g_{\mathrm{I}yy}(\theta) & 0 \\ 0 & 0 & v\{g_{\mathrm{I}xx}(\theta)+g_{\mathrm{I}yy}(\theta)\} \end{bmatrix} + K_{\mathrm{II}} r^{\lambda_{\mathrm{II}}-1} \begin{bmatrix} g_{\mathrm{II}xx}(\theta) & g_{\mathrm{II}xy}(\theta) & 0 \\ g_{\mathrm{II}xy}(\theta) & g_{\mathrm{II}yy}(\theta) & 0 \\ 0 & 0 & v\{g_{\mathrm{II}xx}(\theta)+g_{\mathrm{II}yy}(\theta)\} \end{bmatrix} + K_{\mathrm{III}} r^{\lambda_{\mathrm{III}}-1} \begin{bmatrix} 0 & 0 & g_{\mathrm{III}xz}(\theta) \\ 0 & 0 & g_{\mathrm{III}yz}(\theta) \\ g_{\mathrm{III}xz}(\theta) & g_{\mathrm{III}yz}(\theta) & 0 \end{bmatrix} \tag{4}$$

where v is Poisson's ratio.

Again, it should be emphasized that the orders of singularity λ and the angular profiles of field variables f and g in Eqs. (1)–(4) are functions of material properties and geometrical configuration only. They are independent of the external loadings.

To obtain the orders of singularity and angular profiles, a two-dimensional cross-section orthogonal to the singularity line is considered. Based on the geometry of the material system, the governing elasticity equations for each material and the boundary conditions at the interfaces are written. This system of equations gives rise to an eigenvalue problem with the orders of singularity as eigenvalues and the angular profiles of displacements as eigenfunctions. For a simple geometry, as in the case of a crack in homogeneous medium, analytical solutions for the eigenvalue problem are readily available. However, for a more complicated geometry that involves more than one material with arbitrary sector angles (for example, a square inclusion), a numerical scheme is needed to solve the eigenvalue problem for the orders of singularity and the angular profiles. The formulation and numerical solution for the eigenvalue problem related to the in-plane singularities (mode I and II) are described in details in Lim et al. (2002). A similar approach is used to obtain the solutions for the out-of-plane (mode III) singularity orders and angular profiles (Zhou, 2003).

For the BEM, tractions rather than stresses are used as nodal values. The three-dimensional singular traction field is more complicated than its counterpart in two-dimensional problems. It is not easy to obtain it directly from the eigensolution. However, the traction field can be derived from the singular stress field. The singular traction field in the vicinity of the singularity front associated with a surface can be obtained from

$$\begin{bmatrix} t_x \\ t_y \\ t_z \end{bmatrix} = \begin{bmatrix} \sigma_{xx} & \sigma_{xy} & \sigma_{xz} \\ \sigma_{xy} & \sigma_{yy} & \sigma_{yz} \\ \sigma_{xz} & \sigma_{yz} & \sigma_{zz} \end{bmatrix} \begin{bmatrix} n_x \\ n_y \\ n_z \end{bmatrix} = K_{\mathrm{I}} r^{\lambda_{\mathrm{I}}-1} \begin{pmatrix} p_{\mathrm{I}x}(\theta) \\ p_{\mathrm{I}y}(\theta) \\ p_{\mathrm{I}z}(\theta) \end{pmatrix} + K_{\mathrm{II}} r^{\lambda_{\mathrm{II}}-1} \begin{pmatrix} p_{\mathrm{II}x}(\theta) \\ p_{\mathrm{II}y}(\theta) \\ p_{\mathrm{II}z}(\theta) \end{pmatrix} + K_{\mathrm{III}} r^{\lambda_{\mathrm{III}}-1} \begin{pmatrix} p_{\mathrm{III}x}(\theta) \\ p_{\mathrm{III}y}(\theta) \\ p_{\mathrm{III}z}(\theta) \end{pmatrix} \tag{5}$$

where n_x, n_y and n_z are the components of the normal vector, and $p(\theta)$ is the traction vector representing the angular traction profile. They are given by

$$\begin{pmatrix} p_{\mathrm{I}x}(\theta) \\ p_{\mathrm{I}y}(\theta) \\ p_{\mathrm{I}z}(\theta) \end{pmatrix} = \begin{bmatrix} g_{\mathrm{I}xx}(\theta) & g_{\mathrm{I}xy}(\theta) & 0 \\ g_{\mathrm{I}xy}(\theta) & g_{\mathrm{I}yy}(\theta) & 0 \\ 0 & 0 & v\{g_{\mathrm{I}xx}(\theta)+g_{\mathrm{I}yy}(\theta)\} \end{bmatrix} \begin{bmatrix} n_x \\ n_y \\ n_z \end{bmatrix} \tag{6}$$

$$\begin{pmatrix} p_{\mathrm{II}x}(\theta) \\ p_{\mathrm{II}y}(\theta) \\ p_{\mathrm{II}z}(\theta) \end{pmatrix} = \begin{bmatrix} g_{\mathrm{II}xx}(\theta) & g_{\mathrm{II}xy}(\theta) & 0 \\ g_{\mathrm{II}xy}(\theta) & g_{\mathrm{II}yy}(\theta) & 0 \\ 0 & 0 & v\{g_{\mathrm{II}xx}(\theta)+g_{\mathrm{II}yy}(\theta)\} \end{bmatrix} \begin{bmatrix} n_x \\ n_y \\ n_z \end{bmatrix} \tag{7}$$

$$\begin{pmatrix} p_{\mathrm{III}x}(\theta) \\ p_{\mathrm{III}y}(\theta) \\ p_{\mathrm{III}z}(\theta) \end{pmatrix} = \begin{bmatrix} 0 & 0 & g_{\mathrm{III}xz}(\theta) \\ 0 & 0 & g_{\mathrm{III}yz}(\theta) \\ g_{\mathrm{III}xz}(\theta) & g_{\mathrm{III}yz}(\theta) & 0 \end{bmatrix} \begin{bmatrix} n_x \\ n_y \\ n_z \end{bmatrix} \tag{8}$$

The analytical expressions for the three-dimensional asymptotic displacement and traction fields at the near-tip regions as shown in Eqs. (3) and (5) form the basis to construct the three-dimensional singular boundary elements in Section 4.

3. Formulation of variable-order singular element

In this section, the formulation of a new nine-node singular boundary element is presented. Singular elements replace all the normal elements with three nodes lying on the crack front, as shown in Fig. 2. The displacement and traction fields within the singular element are constructed independently based on the asymptotic fields given in the previous section. However, several polynomial terms including both the constant and linear terms must be added so that rigid body motion is taken into account. The presence of non-singular polynomial fields is important as the singular elements generally need to cover a region substantially larger than the singularity dominant zone.

3.1. Traction field formulation

The construction of traction field within the singular element is elucidated by the element marked by nodes 1–9 lying on the bonded face (Fig. 2). The intrinsic coordinates ξ and η, varying between -1 and 1 within the element, are chosen to lie along the local Cartesian coordinates z' and x' respectively. Hence, the plane strain singular fields lie along the η-direction with the stress intensities varying along the ξ-direction. The traction fields within the singular elements can be expressed as a combination of the singular terms and the non-singular polynomials as

$$t_i = \sum_{h=1}^{3}(a_{1h} + a_{2h}\xi + a_{3h}\xi^2)r^{\lambda_h - 1}p_{ih}(\theta) + a_4 + a_5\xi + a_6\eta + a_7\xi\eta + a_8\xi^2 + a_9\xi^2\eta \tag{9}$$

where t_i is the ith component of the tractions at the coordinate (ξ, η), and a_{ih}, a_i $(i = 1\text{–}9)$ are the independent coefficients to be determined.

The first part in Eq. (9) represents the contribution from the singular fields in which the stress intensity coefficients are assumed to have a quadratic variation along ξ, and the order of singularity λ_h and angular profile $p_{ih}(\theta)$ are assumed to be unchanged along the crack front. The second part which includes a non-

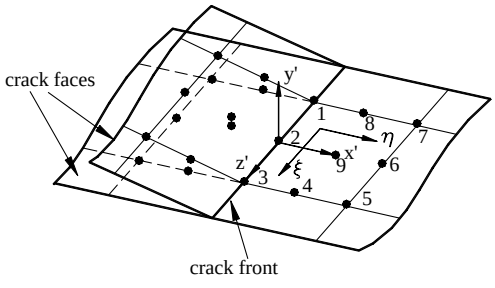

Fig. 2. Typical 3D edge singular element.

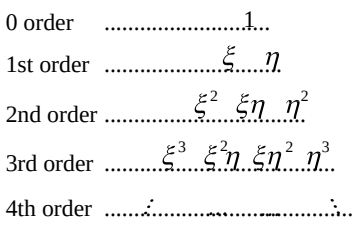

Fig. 3. Pascal triangle.

singular field is obtained according to the sequence in the Pascal triangle, as shown in Fig. 3. The last polynomial term in Eq. (9) is chosen to be $a_9\xi^2\eta$ instead of $a_9\eta^2$, because among all the possible terms including η^2, ξ^3, $\xi^2\eta$, $\xi\eta^2$ and η^3, only the use of the term $\xi^2\eta$ generates a unique solution for all the independent coefficients a_i in Eq. (9) in the procedure shown next.

The coefficients a_i can be expressed in terms of the nodal tractions $t_i^{(m)}$ at the non-singular nodes m ($m = 4$–9) and the stress intensity factors $K_h^{(n)}$ at the singular nodes n ($n = 1$–3 and $h = \mathrm{I}$, II, III denoting the modes). Such relationships are established by substituting the appropriate nodal tractions, stress intensity factors and coordinates (ξ, η) into Eq. (9), forming a system of equations from which the coefficients a_i can be obtained. The expression for describing the traction fields within the singular element is then given by

$$t_i = \sum_{h=1}^{3}(N_{ih}^{(1)}K_h^{(1)} + N_{ih}^{(2)}K_h^{(2)} + N_{ih}^{(3)}K_h^{(3)}) + \sum_{m=4}^{9}N^{(m)}t_i^{(m)} \tag{10}$$

where $N^{(m)}$ ($m = 4$–9) are the shape functions for the non-singular nodes m and $N_{ih}^{(n)}$ ($n = 1, 2, 3$) are the shape functions for the ith component at the singular node n corresponding to the hth mode. These shape functions are given by

$$N_{ih}^{(1)} = \{r^{\lambda_h-1}p_{ih}(\theta) - (1-\eta)[r^{\lambda_h-1}p_{ih}(\theta)]_{\eta=0} - \eta[r^{\lambda_h-1}p_{ih}(\theta)]_{\eta=1}\}(0.5\xi^2 - 0.5\xi) \tag{11}$$

$$N_{ih}^{(2)} = \{r^{\lambda_h-1}p_{ih}(\theta) - (1-\eta)[r^{\lambda_h-1}p_{ih}(\theta)]_{\eta=0} - \eta[r^{\lambda_h-1}p_{ih}(\theta)]_{\eta=1}\}(1-\xi^2) \tag{12}$$

$$N_{ih}^{(3)} = \{r^{\lambda_h-1}p_{ih}(\theta) - (1-\eta)[r^{\lambda_h-1}p_{ih}(\theta)]_{\eta=0} - \eta[r^{\lambda_h-1}p_{ih}(\theta)]_{\eta=1}\}(0.5\xi^2 + 0.5\xi) \tag{13}$$

$$N^{(4)} = (1-\eta)(0.5\xi^2 + 0.5\xi) \tag{14}$$

$$N^{(5)} = \eta(0.5\xi^2 + 0.5\xi) \tag{15}$$

$$N^{(6)} = \eta(1-\xi^2) \tag{16}$$

$$N^{(7)} = \eta(0.5\xi^2 - 0.5\xi) \tag{17}$$

$$N^{(8)} = (1-\eta)(0.5\xi^2 - 0.5\xi) \tag{18}$$

$$N^{(9)} = (1-\eta)(1-\xi^2) \tag{19}$$

The shape functions $N^{(m)}$ (corresponding to the non-singular nodes) are unity at the self-node m and zero at the other nodes. However, the shape functions $N_{ih}^{(n)}$ (corresponding to the singular nodes) are infinite in value at node n and zero at the other nodes.

It is interesting to note that the above formulation can also be obtained by simply employing the Lagrange interpolation. Since the traction field along the η-direction is that of the plane strain solution, it can be directly written by a combination of η-direction singular fields due to three singular modes and linear terms. Using edge 1-8-7 as example and noting η varying from -1 to 1, the traction field along η-direction can be represented by

$$t_i = \sum_{h=1}^{3} \{ r^{\lambda_h - 1} p_{ih}(\theta) - (1-\eta)[r^{\lambda_h - 1} p_{ih}(\theta)]_{\eta=0} - \eta [r^{\lambda_h - 1} p_{ih}(\theta)]_{\eta=1} \} K_h^{(1)} + (1-\eta) t_i^{(8)} + \eta t_i^{(7)} \tag{20}$$

where $K_h^{(1)}$ is the hth component of the stress intensity factors at the singular node ad $t_i^{(8)}$ and $t_i^{(7)}$ are the tractions at the other two non-singular nodes along η-direction. On the other hand, the nodal variables along the ξ-direction, like $K_h^{(1)}$, $t_i^{(8)}$ and $t_i^{(7)}$ are assumed to vary in a quadratic form. For the variation of ξ from -1 to 1, the traction variation along the ξ-direction can be explicitly written by

$$t_i = (0.5\xi^2 + 0.5\xi) t_i^{(5)} + (1-\xi^2) t_i^{(6)} + (0.5\xi^2 - 0.5\xi) t_i^{(7)} \tag{21}$$

where $t_i^{(5)}$, $t_i^{(6)}$, $t_i^{(7)}$ are tractions of node 5-6-7 respectively as shown in Fig. 2. According to the concept of Lagrange interpolation, the traction field within the whole surface singular boundary element can be obtained by the product of the traction tensor along the η-direction shown in Eq. (20) and the traction tensor along the ξ-direction shown in Eq. (21). The result of this Lagrange interpolation is found to be identical to that shown in Eqs. (10)–(19). The details to obtain the formulation by employing the concept of Lagrange interpolation are briefly described in Zhou (2003). The two kinds of formulations have identical results because the singular fields in the plane normal to the crack front are dominated by plane strain singularities, and the singular fields take a similar form in each normal plane with only their intensities varying along the crack front in a quadratic variation.

The singular boundary element based on Eq. (10) is naturally compatible with its neighboring elements. This can be verified as follows. The compatibility requirement for any two elements sharing a common edge is that the field variations of the two elements reduce to the same profile at the common edge. Consider the common edge represented by nodes 5-6-7 shown in Fig. 2 between the singular element and a normal nine-node quadratic element. From Eq. (10), it can be shown that traction variation along this edge from the singular element reduces to exactly Eq. (21). Obviously, Eq. (21) is identical to the formulation on the common edge from a nine-node normal quadratic element. Next, consider the common edge represented by nodes 3-4-5 shown in Fig. 2 shared by two singular elements. The traction variations from both elements along that common edge are identical as given by Eq. (20). Hence, the compatibility conditions are fully satisfied between neighboring singular elements. Since the singular boundary element satisfies the compatibility conditions with its neighboring elements (including both singular and normal quadratic elements), there is no need for transition elements, such as those used for the enriched singular finite element (Pageau and Biggers, 1997).

3.2. Displacement field formulation

Similar to the above traction formulation, the displacement shape functions can also be constructed by employing the concepts of Lagrange interpolation, that is, they are the tensor products of the corresponding one-dimensional interpolation functions. The displacement fields along the ξ-direction of the intrinsic coordinates are assumed to have a quadratic variation, while the plane strain asymptotic singular fields are dominant along the η-direction. In contrast to traction formulation discussed above, there are more alternatives to formulating the displacement fields along the η-direction. These options include the purely quadratic formulation, the formulation with singular and linear terms, and the formulation with singular and quadratic terms.

3.2.1. Purely quadratic terms

Since the nodal values of displacement at the crack front are finite, they can be used directly as the nodal unknowns. In this case, the displacement field along the η-direction within the singular element is assumed to be of a purely quadratic form with no singular terms shown in Eq. (1):

$$u_i = a + b\eta + c\eta^2 \tag{22}$$

Since the displacement field is of a quadratic form in both ξ and η directions, the formulation of the displacement field is the same as a normal nine-node quadratic element. It can be simply written as

$$u_i = \sum_{j=1}^{9} N^{(j)}(\xi,\eta)u_i^{(j)} \tag{23}$$

where $u_i^{(j)}$ is the ith component of the displacements at node j, $N^{(j)}$ are the standard shape functions at node j for normal nine-node quadratic elements, as given in many textbooks (see for example Becker, 1992).

3.2.2. Singular and linear terms

In this case, the displacement field along the η-direction is assumed to contain the asymptotic singular field in addition to the linear terms which represent the non-singular field:

$$u_i = \sum_{h=1}^{s} K_h r^{\lambda_h} f_{ih}(\theta) + a_i + b_i\eta \tag{24}$$

Here, λ and $f(\theta)$ are the eigensolutions as shown in Eq. (1) and a_i and b_i are two independent coefficients in the ith component. Again, Eq. (24) can be written in terms of the unknown nodal displacements at the three nodes along η-direction. In this case, the stress intensity factor K is considered as one of the unknown coefficients. Since the components of the asymptotic displacement angular profiles are not independent of each other, all three components of nodal displacements need to be considered together. The element edge represented by nodes 3-4-5 shown in Fig. 2 is used to illustrate the construction of the displacement formulation along the η-direction. Along this edge ($\xi = 1$), there are nine components of nodal displacements, which correspond to nine independent coefficients including three components of stress intensity factors at node 3 and three components of coefficients a and b, respectively. By specifying appropriate nodal displacements and local coordinates in Eq. (24), a set of linear equations can be established as shown:

$$\begin{Bmatrix} u_x^{(3)} \\ u_y^{(3)} \\ u_z^{(3)} \\ u_x^{(4)} \\ u_y^{(4)} \\ u_z^{(4)} \\ u_x^{(5)} \\ u_y^{(5)} \\ u_z^{(5)} \end{Bmatrix} = \begin{bmatrix} 0 & 0 & 0 & 1 & -1 & 0 & 0 & 0 & 0 \\ 0 & 0 & 0 & 0 & 0 & 1 & -1 & 0 & 0 \\ 0 & 0 & 0 & 0 & 0 & 0 & 0 & 1 & -1 \\ (0.5L)^{\lambda_{\mathrm{I}}} f_{\mathrm{I}x}(\theta) & (0.5L)^{\lambda_{\mathrm{II}}} f_{\mathrm{II}x}(\theta) & 0 & 1 & 0 & 0 & 0 & 0 & 0 \\ (0.5L)^{\lambda_{\mathrm{I}}} f_{\mathrm{I}y}(\theta) & (0.5L)^{\lambda_{\mathrm{II}}} f_{\mathrm{II}y}(\theta) & 0 & 0 & 0 & 1 & 0 & 0 & 0 \\ 0 & 0 & (0.5L)^{\lambda_{\mathrm{III}}} f_{\mathrm{III}z}(\theta) & 0 & 0 & 0 & 0 & 1 & 0 \\ L^{\lambda_{\mathrm{I}}} f_{\mathrm{I}x}(\theta) & L^{\lambda_{\mathrm{II}}} f_{\mathrm{II}x}(\theta) & 0 & 1 & 1 & 0 & 0 & 0 & 0 \\ L^{\lambda_{\mathrm{I}}} f_{\mathrm{I}y}(\theta) & L^{\lambda_{\mathrm{II}}} f_{\mathrm{II}y}(\theta) & 0 & 0 & 0 & 1 & 1 & 0 & 0 \\ 0 & 0 & L^{\lambda_{\mathrm{III}}} f_{\mathrm{III}z}(\theta) & 0 & 0 & 0 & 0 & 1 & 1 \end{bmatrix} \begin{Bmatrix} K_{\mathrm{I}} \\ K_{\mathrm{II}} \\ K_{\mathrm{III}} \\ a_x \\ b_x \\ a_y \\ b_y \\ a_z \\ b_z \end{Bmatrix}$$

$$= [A][K_{\mathrm{I}} \quad K_{\mathrm{II}} \quad K_{\mathrm{III}} \quad a_x \quad b_x \quad a_y \quad b_y \quad a_z \quad b_z]^{\mathrm{T}} \tag{25}$$

where L is the length of edge 3-4-5, and A is the coefficient matrix. Solving this set of linear equations for the unknown coefficients and substituting them back into Eq. (24), the displacement field along the η-direction can be rewritten in terms of the unknown nodal displacements as

$$\begin{Bmatrix} u_x \\ u_y \\ u_z \end{Bmatrix} = \begin{bmatrix} r^{\lambda_{\mathrm{I}}} f_{\mathrm{Ix}}(\theta) & r^{\lambda_{\mathrm{II}}} f_{\mathrm{IIx}}(\theta) & 0 & 1 & \eta & 0 & 0 & 0 & 0 \\ r^{\lambda_{\mathrm{I}}} f_{\mathrm{Iy}}(\theta) & r^{\lambda_{\mathrm{II}}} f_{\mathrm{IIy}}(\theta) & 0 & 0 & 0 & 1 & \eta & 0 & 0 \\ 0 & 0 & r^{\lambda_{\mathrm{III}}} f_{\mathrm{IIIz}}(\theta) & 0 & 0 & 0 & 0 & 1 & \eta \end{bmatrix} [A]^{-1} \begin{Bmatrix} u_x^{(3)} \\ u_y^{(3)} \\ u_z^{(3)} \\ u_x^{(4)} \\ u_y^{(4)} \\ u_z^{(4)} \\ u_x^{(5)} \\ u_y^{(5)} \\ u_z^{(5)} \end{Bmatrix}$$

$$= [M] \begin{bmatrix} u_x^{(3)} & u_y^{(3)} & u_z^{(3)} & u_x^{(4)} & u_y^{(4)} & u_z^{(4)} & u_x^{(5)} & u_y^{(5)} & u_z^{(5)} \end{bmatrix}^{\mathrm{T}} \tag{26}$$

where M is the interpolation matrix. By partitioning M into its sub-matrices as

$$[M] = [M_1, M_2, M_3] \tag{27}$$

the sub-matrices M_1, M_2 and M_3 become the shape functions for nodes 3, 4 and 5, respectively. These shape functions are enriched with the singular displacement field. The displacement field along the η-direction can then be explicitly written as

$$\begin{Bmatrix} u_x \\ u_y \\ u_z \end{Bmatrix} = [M_1] \begin{Bmatrix} u_x^{(3)} \\ u_y^{(3)} \\ u_z^{(3)} \end{Bmatrix} + [M_2] \begin{Bmatrix} u_x^{(4)} \\ u_y^{(4)} \\ u_z^{(4)} \end{Bmatrix} + [M_3] \begin{Bmatrix} u_x^{(5)} \\ u_y^{(5)} \\ u_z^{(5)} \end{Bmatrix} \tag{28}$$

Since the displacement field along the ξ-direction is of a quadratic form, the complete displacement field of the singular boundary element can be constructed by employing the Lagrange interpolation to give

$$u_i = \sum_{j=1}^{9} B^{(j)}(\xi, \eta) u_i^{(j)} \tag{29}$$

where $B^{(j)}(\xi, \eta)$ is the enriched shape function for node j. The details of $B^{(j)}(\xi, \eta)$ are too complicated to be written explicitly here, but it can be easily obtained through matrix operation as shown above.

3.2.3. Singular and quadratic terms

Another alternative formulation for the displacement field is to use the singular field shown in Eq. (1) and the quadratic terms that represent the non-singular field. Thus, along the η-direction, the displacement field is expressed as

$$u_i = \sum_{h=1}^{3} K_h r^{\lambda_h} f_{ih}(\theta) + a_i + b_i \eta + c_i \eta^2 \tag{30}$$

In contrast to Section 3.2.2, the stress intensity factors are no longer considered as unknown independent coefficients but these are the same as those prescribed in the traction formulation. Hence the displacement and traction variations in this element are explicitly coupled through its shape functions. Three independent unknown coefficients a_i, b_i and c_i are used instead. For each component of the displacement fields, there are three unknown nodal displacements corresponding to three independent coefficients a, b and c. Similar to the previous formulation in Section 3.2.2, a set of linear equations can be established to solve for the

coefficients a_i, b_i and c_i, in terms of the nodal values. For example, the displacement field along the η-direction the edge 3-4-5 can be rewritten in terms of the nodal displacements and the nodal stress intensity factors as given by

$$u_i = 0.5\eta(\eta-1)u_i^{(3)} + (1-\eta^2)u_i^{(4)} + 0.5\eta(\eta+1)u_i^{(5)} + \sum_{h=1}^{3}\{r^{\lambda_h-1}f_{ih}(\theta) - (1-\eta^2)\{r^{\lambda_h-1}f_{ih}(\theta)\}_{\eta=0} - (0.5\eta(\eta+1))\{r^{\lambda_h-1}f_{ih}(\theta)\}_{\eta=1}\}K_h^{(3)} \tag{31}$$

The first three terms are the same as the conventional one-dimensional quadratic formulation and the fourth term represents the inclusion of the singular fields.

Since all the field variables including the stress intensity factors and displacements vary in a quadratic manner in the ξ-direction, the complete displacement formulation for the singular boundary element can be obtained by means of Lagrange interpolation as

$$u_i = \sum_{j=1}^{9} N^{(j)}(\xi,\eta)u_i^{(j)} + \sum_{h=1}^{3} 0.5\xi(\xi-1)Q_hK_h^{(1)} + \sum_{h=1}^{3}(1-\xi^2)Q_hK_h^{(2)} + \sum_{h=1}^{3} 0.5\xi(\xi+1)Q_hK_h^{(3)} \tag{32}$$

where $N^{(j)}$ is the conventional nine-node quadratic shape function at node j. $K_h^{(i)}$ is the hth component of the stress intensity factor at node i, and

$$Q_h = r^{\lambda_h-1}f_{ih}(\theta) - (1-\eta^2)[r^{\lambda_h-1}f_{ih}(\theta)]_{\eta=0} - (0.5\eta(\eta+1))[r^{\lambda_h-1}f_{ih}(\theta)]_{\eta=1} \tag{33}$$

The coefficients $K_h^{(i)}$ in Eq. (33) are the nodal values of the stress intensity factors at the crack front, which are those used in the traction formulation given in Eq. (10). Hence, in the final matrix assembly, the matrix entries corresponding to the stress intensity factors have contributions from both the traction and displacement formulations.

3.2.4. Discussions on displacement formulations

All the shape functions in the above three kinds of displacement formulations shown in Eqs. (23), (29) and (33) have the property that they are equal to one at its own node and to zero at the other nodes, except for the function Q_h in Eq. (33) which is zero at every node. This property allows all the three displacement formulations to be easily incorporated into the final boundary element formulation. The three formulations vary in the degree of inclusion of the singular field. The first formulation does not include the singular fields, while the second and the third formulations include the singular fields in an uncoupled and coupled manner. In contrast, the traction formulation in Eq. (10) does not have many variations as the displacement formulation since the tractions at the crack front cannot be used as nodal unknowns, and only the stress intensity factors can be used as appropriate nodal values. Thus, three types of three-dimensional singular boundary elements can be constructed with traction formulation in Eq. (10) combined with a choice of the three displacement formulations. All three types of singular elements have been implemented in the present work, and the results are compared in the third example in Section 6. A system in plane strain condition is simulated by imposing symmetric boundary conditions on the two free surfaces normal to the crack front and the results show that the displacement formulation with singular and linear terms is most accurate and the quadratic formulation with no singular terms is the least accurate. The formulation with singular and linear terms is more accurate than the formulation with singular terms and quadratic terms because the former is less constrained, being uncoupled from the traction formulation. Hence, in the following work, only the results generated by the displacement formulation with the singular and linear terms are reported.

3.3. Coordinate transformation

So far, the above three-dimensional singular element formulations are discussed in the local coordinate system. However, during the assembly of the contributions from the singular elements together with other normal quadratic elements, the global coordinate system is required. In complicated structures such as curved crack problems, the local coordinate system near the front may be different form the global coordinate system. Therefore, transformation of the singular fields from local coordinates to global coordinates for general cases is necessary. It is noted that the expressions for stress intensity factors given in Eqs. (10) and (31) are valid only in the local coordinate system, and must remain as such. In contrast, the nodal tractions in Eq. (10) and the nodal displacements in Eqs. (23), (29) and (31), must be expressed in terms of global nodal values so that assembly can be done correctly for both the singular elements and the normal quadratic elements. Suppose A is the transformation matrix from the local coordinate system ($x'y'z'$) to the global coordinate system (xyz). The traction field shown in Eq. (10) can then be rewritten in terms of global coordinates as

$$\{t\} = A\{t'\} = A[N^{(1)}]\{K^{(1)}\} + A[N^{(2)}]\{K^{(2)}\} + A[N^{(3)}]\{K^{(3)}\} + \sum_{m=4}^{9} A[N^{(m)}]A^{-1}\{t^{(m)}\} \tag{34}$$

where $\{K^{(i)}\}$ is the vector of stress intensity factors at node i in local coordinates, $\{t^{(m)}\}$ is the vector of tractions at node m in global coordinates, and $[N^{(i)}]$ is the vector of shape functions at node i. The transformation matrix A can be obtained from the cosines of the angles between the respective axes of the two coordinate systems.

Similarly, the displacement field in the global system can also be obtained by transforming from the local to the global coordinate systems. For the formulation in Eqs. (23) and (29), the transformations are, respectively, given by

$$\{u\} = A\{u'\} = \sum_{j=1}^{9} A[N^{(j)}]A^{-1}\{u^{(j)}\} \tag{35}$$

$$\{u\} = A\{u'\} = \sum_{j=1}^{9} A[B^{(j)}]A^{-1}\{u^{(j)}\} \tag{36}$$

where $\{u^{(j)}\}$ is the displacement vector in the global system at node j. However, for the formulation in Eq. (31), the stress intensity factors are local values, and the transformation is given by

$$\begin{aligned}\{u\} &= A\{u'\} \\ &= \sum_{j=1}^{9} A[N^{(j)}]A^{-1}\{u^{(j)}\} + 0.5\xi(\xi-1)A\{Q\}\{K^{(1)}\} + (1-\xi^2)A\{Q\}\{K^{(2)}\} + 0.5\xi(\xi+1)A\{Q\}\{K^{(3)}\}\end{aligned} \tag{37}$$

where $\{Q\}$ is the vector of functions Q_h ($h = 1, 2$, and 3).

4. Three-dimensional boundary element method

The new three-dimensional singular boundary element can be easily incorporated into a standard three-dimensional boundary element stress analysis code which uses quadratic elements. The detailed formulation of the boundary element method can be found in textbooks (see, e.g., Becker, 1992). The following

gives a brief outline of the method with the inclusion of the singular elements. For each of the homogeneous domains in the multi-material system, a boundary integral equation governing the elastostatic stress state may be written in the form

$$c_{ij}u_j(p) + \int_\Gamma T_{ij}(P,Q)u_j(Q)\,\mathrm{d}\Gamma = \int_\Gamma U_{ij}(P,Q)t_j(Q)\,\mathrm{d}\Gamma \tag{38}$$

In the above equation, u_i and t_i are the displacements and tractions, respectively, and U_{ij} and T_{ij} are the second-order displacement and traction tensors at a field point Q on the boundary due to a unit point load at the variable point P. These are obtained from the fundamental solution to Kelvin's problem, and in three dimensions are given by

$$U_{ij}(P,Q) = \frac{1}{16\pi\mu(1-v)}\frac{1}{r(P,Q)}\left\{(3-4v)\delta_{ij} + \frac{\partial r(P,Q)}{\partial x_i}\frac{\partial r(P,Q)}{\partial x_j}\right\} \tag{39}$$

$$\begin{aligned} T_{ij}(P,Q) = {} & \frac{-1}{8\pi(1-v)r^2(P,Q)}\frac{\partial r(P,Q)}{\partial n}\left\{(1-2v)\delta_{ij} + 3\frac{\partial r(P,Q)}{\partial x_i}\frac{\partial r(P,Q)}{\partial x_j}\right\} \\ & + \frac{1-2v}{8\pi(1-v)r^2(P,Q)}\left\{\frac{\partial r(P,Q)}{\partial x_i}n_j - \frac{\partial r(P,Q)}{\partial x_j}n_i\right\} \end{aligned} \tag{40}$$

where r is the distance between P and Q, and n_i are the components of the normal to the boundary at Q. The free-term coefficients c_{ij} can be easily evaluated from the fact that Eq. (38) must be valid for rigid body displacement fields.

For a quadratic boundary element, the displacements and tractions can be formulated in terms of shape functions $N^{(c)}(\xi,\eta)$ and nodal values $u_i^{(c)}$, $t_i^{(c)}$ as

$$u_i = \sum_{c=1}^{9} N^{(c)}(\xi,\eta)u_i^{(c)} \tag{41}$$

$$t_i = \sum_{c=1}^{9} N^{(c)}(\xi,\eta)t_i^{(c)} \tag{42}$$

where $N^{(c)}$ are the shape functions of normal nine-node quadratic elements as shown in Eq. (32). By discretizing the surface of the domain and applying Gaussian quadrature, the integral equation (38) can be put into a matrix form as

$$[H]\{u\} = [G]\{t\} \tag{43}$$

where $[H]$ and $[G]$ are the coefficient matrices, and $\{u\}$ and $\{t\}$ are the nodal values of the displacements and tractions, respectively.

When the singular elements are used to replace the normal elements in the vicinity of the crack front, the unknown stress intensity factors take the place of the unknown tractions at the crack front and are put in the vector $\{t\}$. The contributions from the singular elements also appear in the coefficient matrices $[H]$ and $[G]$. Hence, the total number of unknowns when singular elements are used is the same as the case when only normal boundary elements are used. Thus, the problem can be uniquely solved when singular elements are employed.

5. Integration of singular boundary elements

Compared with the finite element method, the integrations in the boundary element method is much more difficult. This is because the integrals in Eq. (38) may become singular even for normal non-singular

boundary elements. The three-dimensional Kelvin solution gives rise to strong singularities when the source point falls on the elements, since it has terms of r^{-1} and r^{-2}. Methods to evaluate the integrals in Eq. (38) accurately for normal non-singular elements have already been established (Becker, 1992; Tan and Lee, 1983). The use of singular elements introduces an additional weak singular part since the shape functions for the singular traction field in Eq. (10) have terms of $r^{\lambda-1}$ ($0 < Re(\lambda) < 1$). The shape function tends to an unbounded value when the field point approaches the crack front. At the same time, strong singular integrals due to terms of r^{-1} and r^{-2} are still present if the source point falls on the singular elements. In this case, strong singular terms and weak singular terms are coupled and they need special consideration.

These singular integrals are bounded and accurate values can be obtained in the same way as normal integrals if the singular term is transformed to a non-singular form. Two steps of coordinate transformations can be done to remove the above two kinds of singular integrals. The first step is a geometrical transformation to remove the strong singular integral caused by the Kelvin solution which is done by subdividing the quadrilateral elements into several triangles and using collapsed bilinear elements for these triangles. The second step is to perform an algebraic transformation to overcome the weak singular integral caused by the shape functions in the singular element. Either one or both these steps need to be taken to remove the singular integrals, depending on whether the source point falls on the singular elements or not.

Case 1: Source point is not on the singular element

In this case, the Kelvin kernels U_{ij} and T_{ij} are not singular. However, when the integration is performed over the singular element, the shape functions N_{ih} in Eq. (10) are singular. In this case, algebraic transformation can be used to convert the singular integrand in Eq. (38) into a non-singular one.

For example, the integral on the right-hand side of Eq. (38) within the singular element can be written as

$$\int_{-1}^{1}\int_{-1}^{1} U(\xi,\eta)\left\{\left(\frac{1+\eta}{2}\right)^{\lambda-1} F(\xi,\eta)\right\} J(\xi,\eta)\,\mathrm{d}\xi\,\mathrm{d}\eta \tag{44}$$

where $U(\xi,\eta)$ is one of the kernels, $J(\xi,\eta)$ is the Jacobian of transformation from global coordinates (x,y,z) to intrinsic coordinates (ξ,η), and $F(\xi,\eta)$ is a bounded function in the singular element. Now, introducing a new variable s related to the local coordinate η by

$$\frac{1+s}{2} = \left(\frac{1+\eta}{2}\right)^{\alpha} \tag{45}$$

where

$$\frac{1}{\alpha} = \begin{cases} 2 & \text{if } \lambda \geqslant 0.5 \\ \left[\frac{1}{Re(\lambda)}\right] + 1 & \text{if } \lambda < 0.5 \end{cases} \tag{46}$$

Eq. (44) becomes

$$\int_{-1}^{1}\int_{-1}^{1} U(\xi,\eta)\left\{\frac{1}{\alpha}\left(\frac{1+s}{2}\right)^{\frac{\lambda-\alpha}{\alpha}} F(\xi,\eta)\right\} J(\xi,\eta)\,\mathrm{d}\xi\,\mathrm{d}s \tag{47}$$

It is seen that the integrand in Eq. (47) is bounded within the singular element. In Eq. (46), the function $[x]$ gives the greatest integer lower than x. A similar treatment can be made on the left-hand side of Eq. (38). Subsequently, standard Gauss quadrature based on the new local coordinates ξ and s can be applied, and the integrals in Eq. (38) can be evaluated accurately.

Case 2: Source point falls on singular element, but not on same node as field point

Here, the kernels U_{ij} and T_{ij} have strong singular terms, $1/r$ and $1/r^2$ respectively, and the shape functions for singular elements have the weak singular term of $r^{\lambda-1}$ ($0 < Re(\lambda) < 1$). Both geometrical and algebraic transformations are used to evaluate the integral.

The first step is to transform the integral in terms of original intrinsic coordinates ξ and η into new intermediate intrinsic coordinates ξ and s in the same way as demonstrated in Case 1. By doing this, the singular part from the singular shape functions is removed. After this transformation, all the field variables as well as the geometry of the singular elements are expressed in terms of the intermediate intrinsic coordinates ξ and s.

Next, the singular element is sub-divided into several triangles. Three possible subdivisions as shown in Fig. 4 are used for the cases when the source point P falls on the corner, middle and center nodes, respectively. In order to improve the integration accuracy, two, four and eight triangles are used, respectively, according to the cases shown in Fig. 4. For each triangle, a degenerate four-node rectangular element with local intrinsic coordinates ψ and γ is used. Two nodes of the rectangular element collapse on the source point P while the other two nodes coincide with the remaining two vertices of the triangle.

The coordinate transformation from the intermediate coordinates ξ and s to the third set of local intrinsic coordinates ψ and γ can be written as

$$\xi(\psi,\gamma) = \sum_{i=1}^{4} L^{(i)}(\psi,\gamma)\xi^{(i)} \tag{48}$$

$$s(\psi,\gamma) = \sum_{i=1}^{4} L^{(i)}(\psi,\gamma)s^{(i)} \tag{49}$$

where $L^{(i)}$ is the standard shape function at node i for a four-node rectangular element as given in most finite element textbooks. The intermediate coordinates $\xi^{(i)}$ and $s^{(i)}$ must be found before the geometrical transformation is carried out. Suppose $\tilde{J}(\psi,\gamma)$ is the Jacobian from the intermediate coordinates (ξ,s) to the local coordinates (ψ,γ). After the two steps, the integral in Eq. (44) then becomes

$$\int_{-1}^{1}\int_{-1}^{1} U(\xi,\eta)\left\{\frac{1}{\alpha}\left(\frac{1+s}{2}\right)^{\frac{\lambda-\alpha}{\alpha}} F(\xi,\eta)\right\} J(\xi,\eta)\tilde{J}(\psi,\gamma)\,\mathrm{d}\psi\,\mathrm{d}\gamma \tag{50}$$

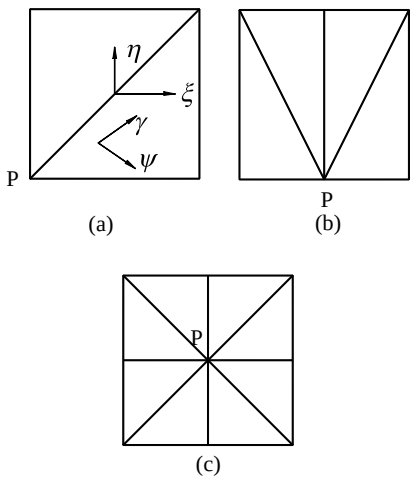

Fig. 4. Sub-division of nine-node three-dimensional boundary element: (a) source point at corner node, (b) source point at middle node, and (c) source point at center node.

In Eq. (50), all singular terms in the singular traction shape functions and the singularities in the kernels are removed. Normal Gauss quadrature can now be employed to accurately evaluate the integral in Eq. (50).

Case 3: Source point falls on singular element, and also on same node as field point

In this last case, the scheme given in Case 2 can be used to evaluate the integral on the right-hand side of Eq. (38) involving the U_{ij} kernel. However, the integral on the left-hand side of Eq. (38) involving the kernel T_{ij} is very difficult to evaluate directly. Fortunately, as in the normal boundary element method, Eq. (38) must be valid for all rigid body movement. This enables the value of the left-hand side integral to be found.

After the appropriate transformations, the singular terms in Eq. (38) are removed and they can be evaluated as normal integrals using standard Gauss quadrature. It should be noted that since Eq. (38) is not made of polynomial terms, the accuracy of the integrals is not as easily achieved as in finite element formulations where 3×3 Gauss points are good enough for nine-node quadratic elements. Here, for the nine-node quadratic boundary elements, up to 8×8 Gauss points are recommended for a satisfactory accuracy.

6. Numerical examples

In this section, five numerical examples are presented to show the versatility and accuracy of the current methodology for solving three-dimensional stress analysis problems with general orders of singularities. The benchmark tests are (i) a penny-shaped crack embedded in an elastic cube, and (ii) a penny-shaped crack embedded at the interface between two dissimilar elastic solids. Analytical results available in the literature are used for comparison. The other three examples with through-thickness cracks and bimaterial inclusion are also investigated. The variations of the stress intensity factors through the thickness are determined. The results based on plane strain conditions for each case are also presented for comparison. For a given problem, appropriate variable-order singular boundary elements are constructed to include the proper singular field based on the preceding singularity analysis. These singular elements are then used along the crack front or inclusion corner to replace those normal elements which are immediately adjacent to the crack front or inclusion corner. The results of stress intensity factors are obtained as nodal values on that line of singularity.

6.1. Penny-shaped crack embedded in an elastic cube

Fig. 5 shows the geometrical configuration of a penny-shaped crack (radius $c = 0.08b$) in a cube with edge b. The Poisson's ratio of the material is taken as 0.3. The boundary element mesh (468 surface

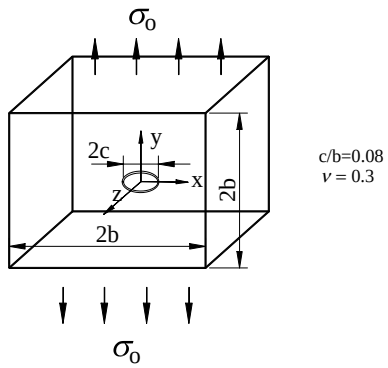

Fig. 5. Penny-shaped crack embedded in an elastic cube.

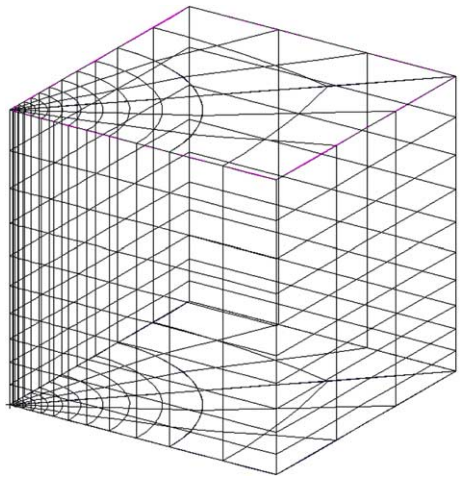

Fig. 6. Boundary element mesh used for one-eighth of cube.

elements in total) used for one-eighth of the cube is shown in Fig. 6. In the vicinity of the crack front, only six singular edge elements on each side of crack front are used. Since the cube is homogeneous and subjected to remote tension σ_o, only mode I is present. Tada et al. (1973) showed that if the elastic cube is assumed to be infinite, the stress intensity factor along the crack front is constant and is given analytically by

$$K_0 = 2\sigma_o\sqrt{\frac{c}{\pi}} \tag{51}$$

The stress intensity factors K_{I} obtained by the current BEM are compared against the theoretical value by plotting the ratio of K_{I}/K_0 as shown in Fig. 7. It can be seen that the present method gives results that are very close to the theoretical value (within 5% error) even when relatively large elements are used.

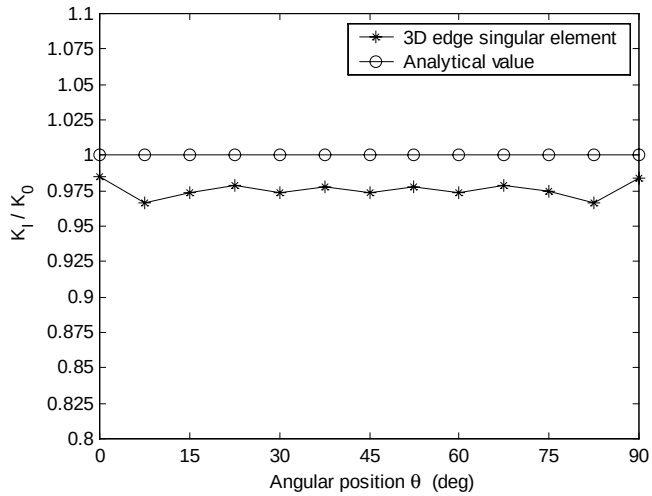

Fig. 7. Normalized mode I stress intensity factor along crack front.

6.2. Penny-shaped crack embedded at interface between two dissimilar elastic solids

In this case, a small penny-shaped crack is embedded at the interface between two big dissimilar elastic solids and subjected to remote tension σ_o. The geometrical configuration and material properties are shown in Fig. 8. Only one-quarter of the problem needs to be modeled due to the symmetry present in the problem. Fig. 9 shows the boundary element mesh (892 surface elements in total) used in the simulation. Again, singular elements are used only for the mesh immediately adjacent to the crack front. Mixed mode stress intensity factors are present in this case due to the material mismatch at the interface. Kassir and Bergman (1972) obtained the analytical solution for the complex stress intensity factors k as

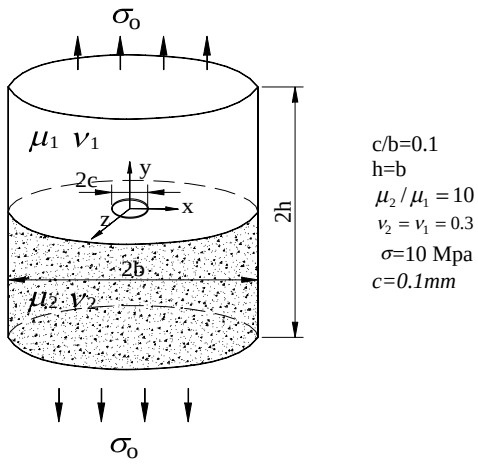

Fig. 8. Penny-shaped crack embedded at interface between two dissimilar elastic solids.

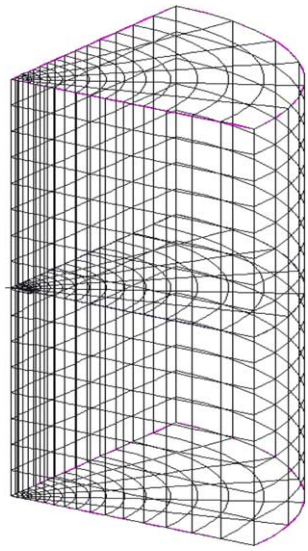

Fig. 9. Boundary element mesh used for one-quarter of problem.

$$k_{\mathrm{I}} + \mathrm{i}k_{\mathrm{II}} = 2\sigma_0\sqrt{c}\,\frac{\Gamma(2+\mathrm{i}\varepsilon)}{\Gamma(0.5+\mathrm{i}\varepsilon)}(2c)^{-\mathrm{i}\varepsilon} \tag{52}$$

where Γ is the gamma function and ε is the bimaterial constant. The term K with dimensions of [stress] [length]$^{0.5}$ is more often used to represent the complex stress intensity factors (Hutchinson and Suo, 1992), and this can be obtained from k by choosing the characteristic length to be $2c$ so that

$$K_{\mathrm{I}} + \mathrm{i}K_{\mathrm{II}} = (k_{\mathrm{I}} + \mathrm{i}k_{\mathrm{II}})(2c)^{\mathrm{i}\varepsilon} = 2\sigma_0\sqrt{c}\,\frac{\Gamma(2+\mathrm{i}\varepsilon)}{\Gamma(0.5+\mathrm{i}\varepsilon)} \tag{53}$$

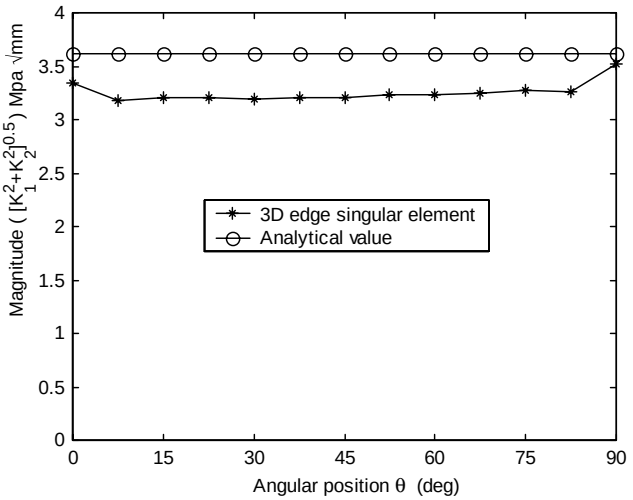

Fig. 10. Magnitude of complex stress intensity factor along crack front.

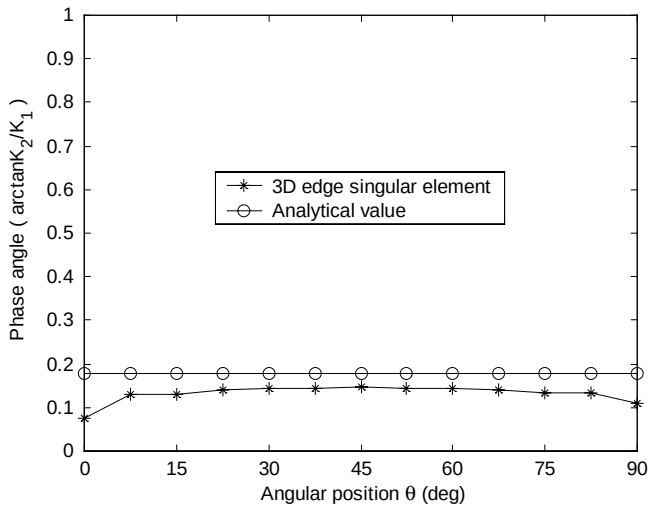

Fig. 11. Phase angle of complex stress intensity factors along crack front.

The theoretical complex stress intensity factors K can also be expressed by its magnitude $|K| = \sqrt{K_{\mathrm{I}}^2 + K_{\mathrm{II}}^2}$ and its phase angle $\varphi = \arctan(K_{\mathrm{II}}/K_{\mathrm{I}})$. The numerical results obtained by using the new three-dimensional variable-order singular elements are shown in Figs. 10 and 11, for the magnitude and the phase angle respectively. The analytical result is also presented for comparison. The results are relatively close, with an error of about 20%. This error can further be reduced by using a finer mesh along the crack front.

6.3. Thin homogeneous plate with a through-thickness crack

A thin homogeneous plate with a through-thickness crack with configuration shown in Fig. 12 under remote tension σ_o is simulated. Only one-eighth of the plate is modeled due to symmetry present in the problem. The boundary mesh (768 surface elements in total) is shown in Fig. 13. In order to verify the accu-

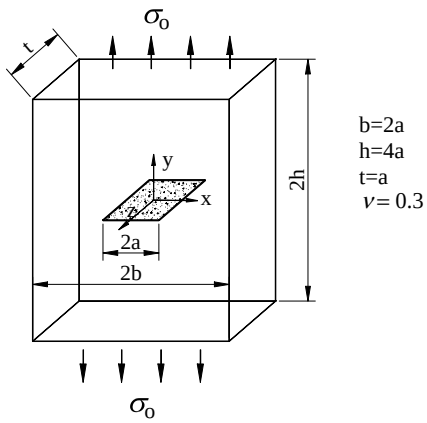

Fig. 12. Thin homogeneous plate with a through-thickness crack.

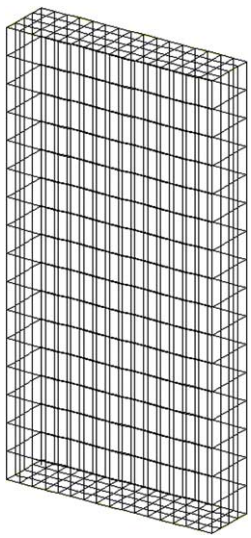

Fig. 13. Boundary element mesh used for one-eighth of problem.

racy of the present method for three-dimensional stress singularity analysis, a loading under plane strain condition is simulated by imposing symmetric boundary conditions on both free surfaces that intersect the crack front. The three types of singular elements with the different displacement formulations described in Section 3.2 are used in turn. Fig. 14 shows the results from these three types of singular elements. The analytical result for the cracked plate under plane strain is given by Tada et al. (1973) as

$$K_{\mathrm{I}} = K_0 f_{\mathrm{geo}}(a, b, h) \tag{54}$$

where $K_0 = \sigma_0\sqrt{\pi a}$, f_{geo} is the geometric correction factor which is equal to 1.19 for this case, and a is the half-crack length. The plane strain condition can also be simulated directly by using the two-dimensional singular element method (Lim et al., 2002). This result is included in Fig. 14 as "2D simulation". Fig. 14 shows that all three displacement formulations give satisfactory results. Among them, the formulation with singular and linear terms is the most accurate one. The error is below 1% along the crack front. It can be seen from Fig. 14 that both two-dimensional singular elements and three-dimensional singular elements give very accurate results. The small differences between the results are very likely due to the fact that the three-dimensional simulation inherently provides a through-thickness variation while the two-dimensional simulation does not. Fig. 15 shows the three-dimensional results for the stress intensity factors when the symmetry conditions are removed from the free surface at $z/t = 0.5$. The present analysis gives results that are in good agreement with Kwon and Sun (2000) who analyzed the same problem using the domain interaction integral method. It is expected that the stress intensity factor decreases when the crack front approaches the free surface at $z/t = 0.5$, since this region is dominated by the corner singularity which usually is weaker than the internal near-tip field (Benthem, 1977).

6.4. Thick bimaterial plate with a through-thickness interface crack

A bimaterial plate with a through-thickness crack along the interface as shown in Fig. 16 under remote tension σ_o is simulated. Fig. 17 shows the boundary element mesh (576 surface elements in total) for the quarter-model of the plate. The bimaterial plate is subdivided into two regions in which each region is made of one homogeneous material. Each region is discretized into surface meshes and the interface mesh is shared by the two regions. The results for the complex stress intensity factors are expressed in terms of their

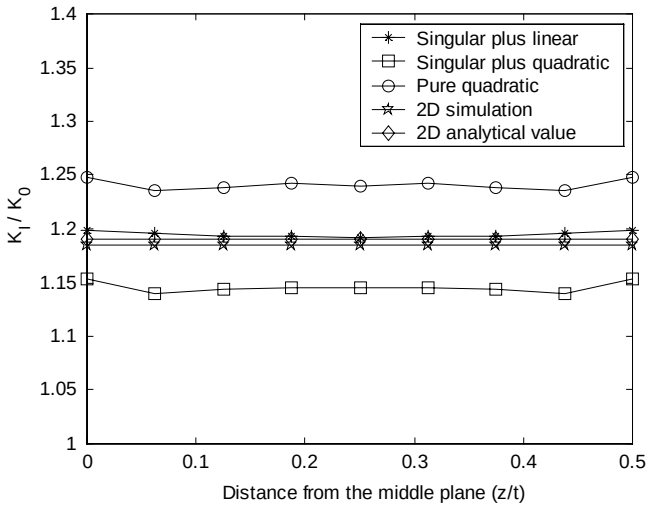

Fig. 14. Normalized mode I stress intensity factor along crack front with symmetry conditions imposed on both free surfaces.

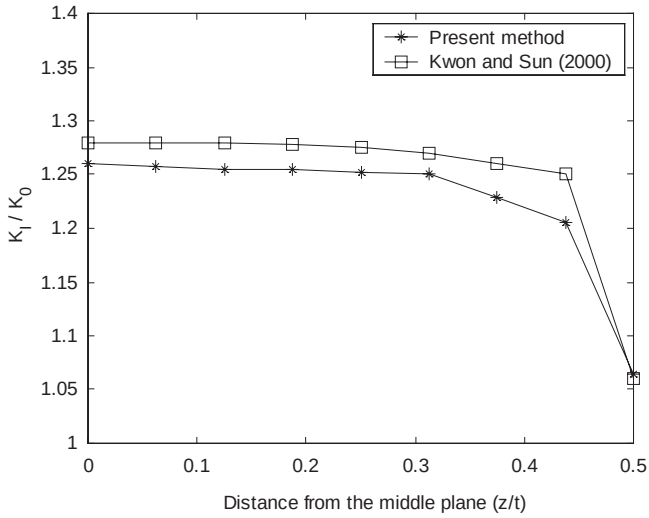

Fig. 15. Normalized mode I stress intensity factor along crack front with surface at $z/t = 0.5$ traction-free.

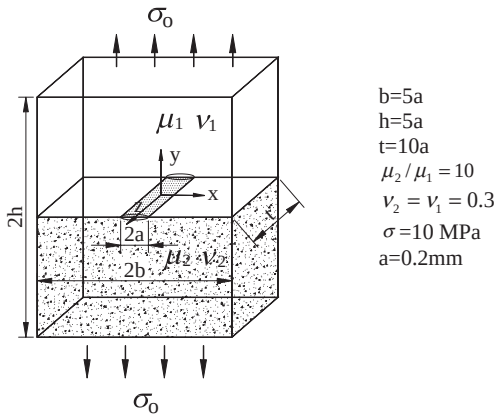

Fig. 16. Thick bimaterial plate with a through-thickness interface crack.

magnitudes and phase angles given in Figs. 18 and 19, respectively. The plane strain conditions are simulated by imposing symmetric boundary conditions on both free surfaces at $z/t = 0$ and $z/t = 0.5$. The results are compared with those obtained by using the two-dimensional singular element method with a similar mesh and very good agreement is obtained. When the surface at $z/t = 0.5$ is made traction-free, a three-dimensional stress state is induced. The corresponding stress intensity factors are plotted in Figs. 18 and 19. The figures show that the results are almost the same as the plane strain solution away from the free surface. Near the corner where the crack front intersects the free surface, the magnitudes and phase angles increase and decrease, respectively. This can be explained by the fact that the bimaterial plate is relatively thick, and plane strain condition dominates along most of the crack front. At the corner where the crack front intersects the free surface, the corner singularities with orders $\lambda_1 = 0.512$ and $\lambda_2 = 0.372$ (Benthem, 1977) are present in the stress field. The stronger corner singularity ($\lambda_1 = 0.512$) causes the increase in mag-

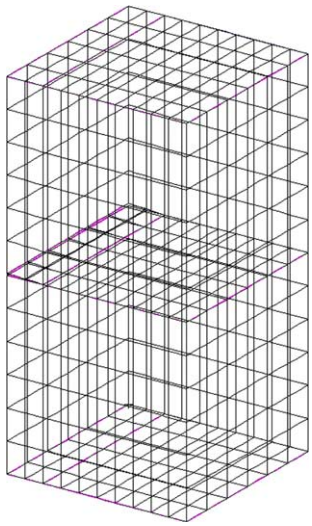

Fig. 17. Boundary element mesh used for one-quarter of problem.

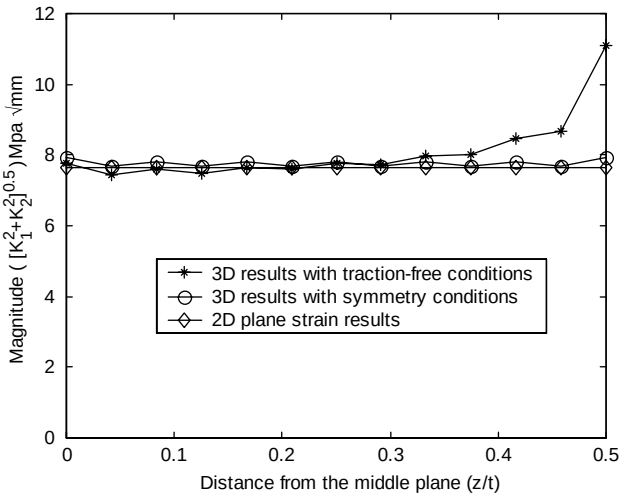

Fig. 18. Magnitude of complex stress intensity factor along crack front.

nitude of the computed stress intensity factor when the corner is approached. It is also noticed that the phase angle decreases to zero at the corner, which is consistent with the corner singularity being a real number. However an accurate analysis for the corner needs to be based upon an appropriate corner singular element which takes the corner singularities into consideration.

6.5. Through-thickness bimaterial inclusion

A bimaterial system with a through-thickness inclusion as shown in Fig. 20 under remote tension σ_o is simulated. Only one-eighth of the block is modeled. Fig. 21 shows the boundary element mesh (448 surface

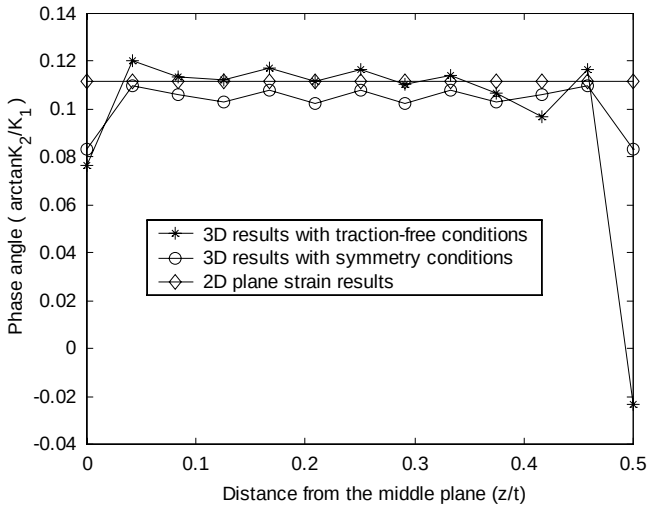

Fig. 19. Phase angle of complex stress intensity factor along crack front.

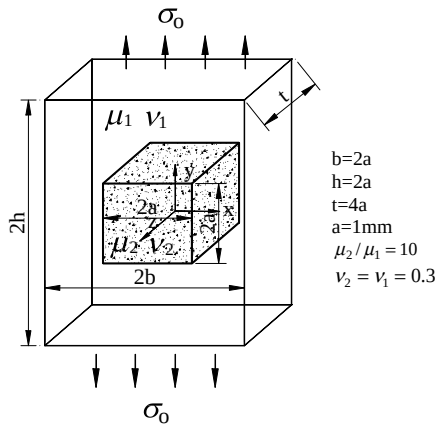

Fig. 20. Through-thickness bimaterial inclusion.

elements in total) for both materials. Two regions are created for the materials. Fig. 22 shows the mesh for the inclusion. Within one-eighth of the plate, there are two interfaces, namely, the horizontal and vertical interfaces. These two interfaces share a common internal bimaterial edge. Even though all the interfaces in this case are fully bonded and no crack is present, singular fields occur near the internal edge due to the material mismatch (Chen, 1994). In this case, the domain integral method may not be applicable since there is no crack. However, the method developed in the current work may be easily applied to this singularity problem as the orders of singularities are known and the displacement and traction profiles along the horizontal and the vertical interfaces can be incorporated into the shape functions of the singular elements. The orders of singularities corresponding to modes I, II and III are found to be 0.798, 0.786 and 0.732, respectively (using the method described by Lim et al., 2002). A new stress intensity factor F is introduced here. At a point on the internal edge, the traction T_y and T_z on the horizontal interface can be defined by

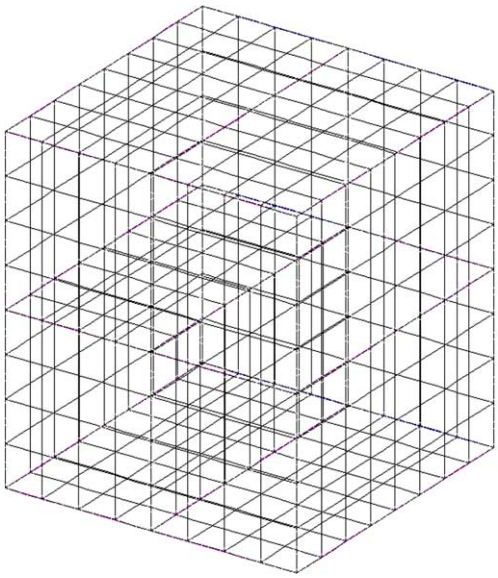

Fig. 21. Boundary element mesh used for one-eighth of problem.

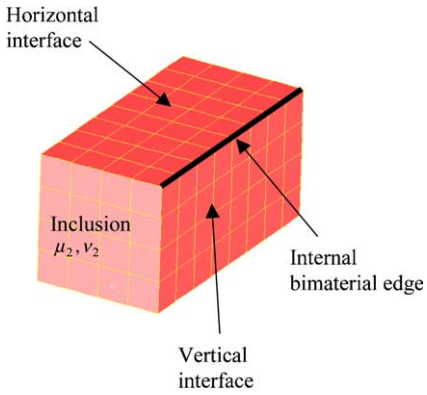

Fig. 22. Boundary element mesh used for inclusion.

$$T_y = r^{\lambda_{\mathrm{I}}-1} F_{\mathrm{I}} \sigma_0 + r^{\lambda_{\mathrm{II}}-1} F_{\mathrm{II}} \sigma_0 \tag{55}$$

$$T_z = r^{\lambda_{\mathrm{III}}-1} F_{\mathrm{III}} \sigma_0 \tag{56}$$

where

$$F_{\mathrm{I}} = K_{\mathrm{I}} p_{\mathrm{I}y}(\theta)|_{\theta=\pi}/\sigma_0 \tag{57}$$

$$F_{\mathrm{II}} = K_{\mathrm{II}} p_{\mathrm{II}y}(\theta)|_{\theta=\pi}/\sigma_0 \tag{58}$$

$$F_{\mathrm{III}} = K_{\mathrm{III}} p_{\mathrm{III}z}(\theta)|_{\theta=\pi}/\sigma_0 \tag{59}$$

where K_{I}, K_{II} and K_{III} are the nodal values of the stress intensity factors and σ_0 is the remote tension. The new stress intensity coefficient F_h has dimension of $a^{1-\lambda_h}$ where a is the half-length of dissimilar inclusion edge and

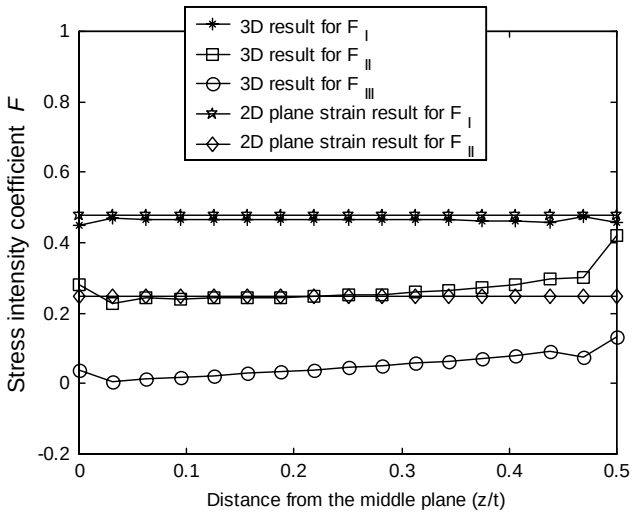

Fig. 23. Stress intensity coefficients along bimaterial inclusion edge.

h refers to modes I to III. The results for three modes of *F* are shown in Fig. 23. Two-dimensional simulations are also carried out with meshes of equivalent fineness, and the results are also plotted in Fig. 23. It is found that the three-dimensional results for modes I and II are very close to the plane strain solutions for most of the internal edges, while the intensity for mode III increases from the mid-plane to the free surface.

7. Conclusions

In this paper, a new three-dimensional variable-order singular boundary element is developed for three-dimensional stress singularity problems. The new singular element incorporates both the variable orders and the angular field variables (displacement and traction variations) along the line of singularities. Hence it can provide a very accurate description of the three-dimensional stress singularities. By using the new singular boundary element, the variations of the stress intensity factors of the three singular modes (two in-plane and one out-of-plane) along the line of singularities are determined. Different displacement formulations including just quadratic terms, singular with linear terms, and singular with quadratic terms, are investigated. The formulation with singular and linear terms is found to be the most accurate. These elements can be used for both straight and curved crack fronts, as well as bimaterial inclusion corners. The methodology is verified by solving embedded penny-shaped homogeneous and bimaterial interface crack problems where closed-form solutions are available and satisfactory agreements are achieved. Simulation on through-thickness bimaterial interface crack and through-thickness bimaterial inclusion problems are also performed. The stress intensity factors which are normally difficult to determine using conventional numerical techniques are easily computed with good accuracy using relatively coarse elements. The new singular boundary element developed here proved to be efficient and robust for solving three-dimensional stress singularity problems.

References

Aliabadi, M.H., 1997. A new generation of boundary element methods in fracture mechanics. International Journal of Fracture 86, 91–125.

Barsoum, R.S., 1976. On the use of isoparametric finite elements in linear fracture mechanics. International Journal for Numerical Methods in Engineering 10, 25–37.

Becker, A.A., 1992. The Boundary Element Method in Engineering—A Complete Course. McGraw-Hill Book Co., London.

Benthem, J.P., 1977. State of stress at the vertex of a quarter-infinite crack in a half-space. International Journal of Solids and Structures 13, 479–492.

Chen, D.H., 1994. Analysis of singular stress-field around the inclusion corner tip. Engineering Fracture Mechanics 49, 533–546.

Cisilino, A.P., Aliabadi, M.H., 1999. Three-dimensional boundary element analysis of fatigue crack growth in linear and non-linear fracture problems. Engineering Fracture Mechanics 63, 713–733.

Cruse, T.A., Vanburen, W., 1971. Three-dimensional elastic stress analysis of a fracture specimen with an edge crack. International Journal of Fracture Mechanics 7, 1–16.

Gosz, M., Dolbow, J., Moran, B., 1998. Domain integral formulation for stress intensity factor computation along curved three-dimensional interface cracks. International Journal of Solids and Structures 35, 1763–1783.

Gray, L.J., Phan, A.-V., Paulino, G.H., Kaplan, T., 2003. Improved quarter-point crack tip element. Engineering Fracture Mechanics 70, 269–283.

Hartranft, R.J., Sih, G.C., 1969. The use of eigenfunction expansions in the general solution of three-dimensional crack problems. Journal of Mathematics and Mechanics 19, 123–138.

Henshell, R.D., Shaw, K.G., 1975. Crack tip finite elements are unnecessary. International Journal for Numerical Methods in Engineering 9, 495–507.

Hutchinson, J.W., Suo, Z., 1992. Mixed mode cracking in layered materials. Advances in Applied Mechanics 29, 63–191.

Kassir, M.K., Bergman, A.M., 1972. The stress intensity factor for a penny-shaped crack between two dissimilar materials. Journal of Applied Mechanics 39, 308–310.

Kwon, S.W., Sun, C.T., 2000. Characteristics of three-dimensional stress fields in plates with a through-the-thickness crack. International Journal of Fracture 104, 291–315.

Li, F.Z., Shih, C.F., Needlemann, A., 1985. A comparison of methods for calculating energy release rate. Engineering Fracture Mechanics 21, 405–421.

Lim, W.K., Kim, S.C., 1994. Further study to obtain a variable power singularity using quadratic isoparametric elements. Engineering Fracture Mechanics 47, 223–228.

Lim, K.M., Lee, K.H., Tay, A.A.O., Zhou, W., 2002. A new variable-order singular boundary element for stress analysis. International Journal for Numerical Methods in Engineering 55, 293–316.

Moran, B., Shih, C.F., 1987a. Crack tip and associated domain integrals from momentum and energy balance. Engineering Fracture Mechanics 27, 615–642.

Moran, B., Shih, C.F., 1987b. A general treatment of crack tip contour integrals. International Journal of Fracture 35, 295–310.

Mustoe, G.G.W., 1980. A combination of the finite element method and the boundary integral procedure for continuum problems. PhD Thesis, University College, Swansea.

Nakamura, T., Parks, D.M., 1988. Three-dimensional stress field near the crack front of a thin elastic plate. Journal of Applied Mechanics 55, 805–813.

Nakamura, T., Parks, D.M., 1989. Antisymmetrical 3-D stress fields near the crack front of a thin elastic plate. International Journal of Solids and Structures 25, 1411–1426.

Pageau, S.S., Biggers, S.B., 1997. Enrichment of finite elements with numerical solutions for singular stress fields. International Journal for Numerical Methods in Engineering 40, 2693–2713.

Shih, C.F., Asaro, R.J., 1988. Elastic plastic analysis of cracks on bimaterial interfaces: Part I—Small scale yielding. Journal of Applied Mechanics 55, 299–316.

Tada, H., Paris, P.C., Irwin, G.R., 1973. The Stress Analysis of Cracks Handbook. Del Research Corporation, Hellertown.

Tan, C.L., Gao, Y.L., 1990. Treatment of biomaterial interface crack problems using the boundary element method. Engineering Fracture Mechanics 36, 919–932.

Tan, C.L., Lee, K.H., 1983. Elastic-plastic stress analysis of a cracked thick-walled cylinder. Journal of Strain Analysis 18, 253–260.

Tracey, D.M., Cook, T.S., 1977. Analysis of power type singularities using finite elements. International Journal for Numerical Methods in Engineering 11, 225–233.

Walker, S.P., Fenner, R.T., 1989. Treatment of corners in BIE analysis of potential problems. International Journal for Numerical Methods in Engineering 28, 2569–2581.

Zhou, W., 2003. Variable-order singular boundary elements for two- and three-dimensional stress analysis with applications in fracture mechanics. PhD Thesis, National University of Singapore.